Precise Measurement of the Cosmic-Ray Spectrum and ⟨ln A⟩ by LHAASO: Connecting the Galactic to the Extragalactic Components

Xing-Jian Lv[1,2] ⬥, Xiao-Jun Bi[1,2,3] ⬥, Kun Fang[1] ⬥, Yi-Qing Guo[1] ⬥, Hui-Hai He[1,2,3] ⬥, Ling-Ling Ma[1,3], Peng-Fei Yin[1],
Qiang Yuan[4] ⬥, and Meng-Jie Zhao[1,5] ⬥

[1] Key Laboratory of Particle Astrophysics, Institute of High Energy Physics, Chinese Academy of Sciences, Beijing 100049, People's Republic of China
[2] University of Chinese Academy of Sciences, Beijing 100049, People's Republic of China
[3] Tianfu Cosmic Ray Research Center, 610000 Chengdu, Sichuan, People's Republic of China
[4] Key Laboratory of Dark Matter and Space Astronomy & Key Laboratory of Radio Astronomy, Purple Mountain Observatory, Chinese Academy of Sciences,
210023 Nanjing, Jiangsu, People's Republic of China
[5] China Center of Advanced Science and Technology, Beijing 100190, People's Republic of China

Abstract

Recently, the LHAASO Collaboration has provided precise measurements of the cosmic rays (CRs) all-particle energy spectrum and mean logarithmic mass ⟨ln A⟩ from 0.3 to 30 PeV. Combining the CR measurements by AMS-02 and DAMPE in space and those by LHAASO and Auger on the ground, we construct a model to recover all these measurements from tens of GeV to tens of EeV. We find that the LHAASO measurement is crucial in the model construction by connecting the Galactic component to the extragalactic component. The precise measurements of CR spectra for individual species by AMS-02 and DAMPE together with the newest LHAASO results clearly indicate three Galactic CR components, that is, a soft low-energy background, a hard high-energy component, and a local source contribution. However, the LHAASO data show that above ∼10^{16} eV, a nonnegligible extra component, possibly of extragalactic origin, must be included. Combining the Auger results and the LHAASO results, we figure out the extragalactic CRs that need at least two components at lower and higher energies. Thanks to the measurements by LHAASO, the constraints on the model parameters are quite stringent. The spectrum features and mass measurements in all energy ranges are all well reproduced in the model.

Unified Astronomy Thesaurus concepts: Cosmic rays (329); Cosmic ray sources (328); Galactic cosmic rays (567); Ultra-high-energy cosmic radiation (1733); Particle astrophysics (96)

1. Introduction

More than a century has passed since Victor Hess's groundbreaking balloon experiment in 1912 (V. F. Hess 1912), yet the origins and characteristics of cosmic rays (CRs) remain enigmatic (J. Becker Tjus & L. Merten 2020). CRs span an immense energy range, from below 10^8 eV up to more than 10^{20} eV. By our current understanding, most of the CRs up to approximately 10^{17} eV originate within our Galaxy, likely linked to supernova events, while CRs with energies higher than about 10^{18} eV are generally considered to be of extragalactic origin, produced from more extreme processes like active galactic nuclei or gamma-ray bursts. The precise energy threshold marking the transition from Galactic to extragalactic sources remains a subject of ongoing debate (R. A. Batista et al. 2019).

Based on the theory of diffusive shock acceleration (L. O. Drury 1983) and CR propagation as a diffusive process (A. W. Strong et al. 2007), CRs are traditionally understood to exhibit a power-law spectrum. The feature known as "the knee" is ascribed to the Peters cycle (B. Peters 1961), reflecting the maximum energy attainable by Galactic CR sources. However, recent spaceborne experiments have unveiled several unexpected features in the CR spectrum. These anomalies include a hardening at ∼200 GV across most of the primary CR spectra (A. D. Panov et al. 2007, 2009; H. S. Ahn et al. 2010;

O. Adriani et al. 2011; M. Aguilar et al. 2015a, 2015b; Y. S. Yoon et al. 2017), a softening at ∼10 TV in the spectra of protons and helium (Y. S. Yoon et al. 2017; E. Atkin et al. 2018; Q. An et al. 2019; F. Alemanno et al. 2021), and a subsequent hardening at ∼100 TeV in the combined proton and helium spectrum (F. Alemanno et al. 2024). Concurrently, ground-based experiments have validated the well-established knee at roughly 4 PeV, the ankle around 5 EeV, and the suppression at 40 EeV while also uncovering new phenomena: a low-energy (LE) ankle at 2×10^{16} eV (M. G. Aartsen et al. 2013; V. V. Prosin et al. 2016) and a second knee at around 10^{17} eV (see D. R. Bergman & J. W. Belz 2007 for a review).

Recently, the Large High Altitude Air Shower Observatory (LHAASO) published measurements of the all-particle CR energy spectrum and the mean logarithmic mass of CRs with unprecedented accuracy in 0.3–30 PeV (Z. Cao et al. 2024). The mean logarithmic mass shows a nonmonotonic change with energy, a phenomenon observed for the first time.

Phenomenological studies have been conducted utilizing data available at different times (J. R. Hörandel 2003; A. M. Hillas 2006; V. I. Zatsepin & N. V. Sokolskaya 2006; T. K. Gaisser et al. 2013; T. Stanev et al. 2014; S. Thoudam et al. 2016; H. P. Dembinski et al. 2018; Y.-Q. Guo & Q. Yuan 2018; C. Yue et al. 2019). H. P. Dembinski et al. (2018) compiled the most up-to-date data available then, spanning a broad energy spectrum. However, their approach, a global spline fit, is entirely data-driven and provides no information on the specific populations contributing to the observed spectrum and compositions. Consequently, this study revisits the phenomenological modeling of CRs, covering a comprehensive energy range

from tens of GeV/Z, an energy range where solar modulation effects are negligible (M. S. Potgieter 2013), up to 10^{11} GeV, the highest detectable energies.

The LHAASO measurements on the spectrum and $\langle \ln A \rangle$ around the knee are important for constraining our model. At the lower-energy limit of its measurements, the influence of an assumed local source, which is hypothesized to be responsible for the spectral bump detected by spaceborne experiments around 10 TV (Q. An et al. 2019; F. Alemanno et al. 2021), remains pronounced. Notably, the cutoff in the iron component from the local source contributes to the observed decrease in $\langle \ln A \rangle$ by LHAASO for the first time. For the higher energies, LHAASO's measurements of both the all-particle spectrum and $\langle \ln A \rangle$ around the knee strongly indicate a "light knee" resulting from the sequential cutoff of Galactic protons and helium. At the uppermost energies of LHAASO, the emergence of the LE ankle helps to constrain the LE end of a possible extragalactic component.

In addition to the latest LHAASO measurements, we have also included data from other major modern space-based and ground-based experiments to cover a wide range of energies. This is possible since no specific modern data strongly disagree with each other after energy rescaling and accounting for systematic errors. Our model, however, tends to favor the central values measured by LHAASO due to its enhanced precision compared to other experiments. The details of the data sets and our model are presented in Section 2. The results and their implications are discussed in Section 3. Finally, we summarize our findings in Section 4.

2. The Model Construction

We first compile all the CR data from the major modern space-based and ground-based experiments. We assume that the spectral discrepancy between any two measurements with overlap energies is attributed to the absolute energy calibration of the two experiments. By slightly adjusting the energy scale, we calibrate the absolute energies of all experiments with AMS-02. Then we get a CR spectrum from GeV to tens of EeV. Our model is then constructed to reproduce the whole energy spectrum.

We find that incorporating three Galactic components can provide a satisfactory agreement with the data: a local source and two background populations, referred to as Population I (Pop. I) and Population II (Pop. II). Meanwhile, the extragalactic contributions are composed of two populations, i.e., the LE and high-energy (HE) populations. The spectrum of each population is assumed to be a power law with an exponential cutoff, as detailed in Section 2.2. The cutoff energies of different species of each population depend on the atomic number Z, a natural consequence if the cutoff originates from acceleration or propagation processes (J. R. Hörandel 2003).

2.1. Data Compiled

For spaceborne experiments, we opt to use the latest results by AMS-02 (M. Aguilar et al. 2020), DAMPE (Q. An et al. 2019), and CALET (O. Adriani et al. 2022). The AMS-02 data set is presented in terms of rigidity, whereas the DAMPE and CALET data are expressed as total kinetic energy. To compare with ground-based experiments, a conversion to total energy is needed. We assume that the flux is dominated by a single isotope except

for helium,[6] where the fitted function of AMS-02 (M. Aguilar et al. 2019) for the ^{3}He/^{4}He ratio is used to achieve an accurate conversion. Furthermore, the DAMPE measurement of proton plus helium (p+He) is converted using the ratio derived from the DAMPE proton and helium spectrum. We checked that adopting a 50/50 split, as done in the DAMPE p+He study, does not significantly alter the results. Additionally, when measurements from AMS-02, DAMPE, or CALET are unavailable, data from NUCLEON (V. Grebenyuk et al. 2019) are employed.

Spaceborne experiments lack sufficient statistics above 10^5 GeV, necessitating the use of ground-based experiments due to their larger acceptance. Besides the latest measurements of the all-particle spectrum and $\langle \ln A \rangle$ made by LHAASO, we include data from all major modern ground-based experiments, as follows: the High Altitude Water Cherenkov (HAWC; J. A. Morales-Soto et al. 2021), IceCube-IceTop (M. G. Aartsen et al. 2020), KASCADE (W. D. Apel et al. 2013), KASCADE-Grande (W. D. Apel et al. 2013), the Pierre Auger Observatory (P. Abreu et al. 2021), the Telescope Array (TA; D. Ivanov 2020), the TA Low Energy Extension (TALE; R. U. Abbasi et al. 2018b), Tibet-III (M. Amenomori et al. 2008), and TUNKA-133 (V. Prosin et al. 2014).[7]

Data taken by different experiments often have systematic discrepancies. Following previous works (J. R. Hörandel 2003; T. K. Gaisser et al. 2013; T. Stanev et al. 2014; H. P. Dembinski et al. 2018), we attribute these discrepancies to an energy-scale offset $\tilde{E} = \delta \times E$, where $\tilde{E}$ is the measured energy and E is the true energy. Consequently, the reported differential flux $\tilde{\phi}(\tilde{E})$ and the true differential flux $\phi(E)$ are related by $\tilde{\phi}(\tilde{E}) = \phi(E) dE/d\tilde{E} = \phi(\tilde{E}/\delta)\delta^{-1}$. The value of δ is determined to minimize the deviation between experiments a and b, which is quantified by

$$\chi^2_{ab}(\delta_b) \equiv \sum_i \frac{(\mathcal{D}_a(E_i) - \mathcal{D}_b((\delta_b E)_i))^2}{\sigma^2_a(E_i) + \sigma^2_b((\delta_b E)_i)} , \qquad (1)$$

where the summation runs over the overlapping energy range between experiments a and b. Given that the energy bins are different for different experiments, we use the energy bins of experiment a as a reference and accordingly interpolate both $\mathcal{D}_b(\delta_b E_b)$ and $\sigma^2_b(\delta_b E_b)$. The AMS-02 data serve as the benchmark for energy calibration, benefiting from its precise energy calibration enabled by its permanent magnet. Subsequently, the CALET, DAMPE, and NUCLEON data sets are calibrated against the corresponding AMS-02 data. The minimization package iminuit (Version 2.25.2; F. James & M. Roos 1975; H. Dembinski et al. 2024) is adopted to optimize δ for spaceborne experiments, with the results summarized in Table 1.

---

[6] This assumption disregards isotopic variations because, for protons, ^{1}H dominates over ^{2}H by orders of magnitude (O. Adriani et al. 2016), and for elements heavier than helium, such as carbon, the mass differential between isotopes (e.g., ^{12}C versus ^{13}C) is relatively minor. Helium is an exception, as its isotopes, ^{3}He and ^{4}He, not only share comparable fluxes but also exhibit a substantial relative mass difference.

[7] The choice of hadronic model can significantly influence the measured spectrum. We use the latest version of QGSJETII as provided by the experimental groups, except in the case of Auger data, for which we choose the EPOS-LHC results due to the Auger collaboration's demonstration that outcomes derived using QGSJETII were unphysical (E. W. Mayotte et al. 2023).

Table 1
Summary of Energy Calibration for Spaceborne Experiments

Experiment	δ	References
AMS-02	1.00	M. Aguilar et al. (2020)
DAMPE proton	0.987 ± 0.017	Q. An et al. (2019)
DAMPE helium	1.037 ± 0.025	F. Alemanno et al. (2021)
DAMPE p+He	1.029 ± 0.025	F. Alemanno et al. (2024)
NUCLEON C and O	1.026 ± 0.034	V. Grebenyuk et al. (2019)
NUCLEON Ne and Mg and Si	1.18 ± 0.05	V. Grebenyuk et al. (2019)
NUCLEON iron	1.28 ± 0.08	V. Grebenyuk et al. (2019)
CALET proton	1.019 ± 0.012	O. Adriani et al. (2022)
CALET helium	1.022 ± 0.015	O. Adriani et al. (2023)
CALET C and O	1.155 ± 0.009	O. Adriani et al. (2020)
CALET iron	1.113 ± 0.008	O. Adriani et al. 2021)

Table 2
Summary of Energy Calibration for Ground-based Experiments

Experiment	δ	References
HAWC	0.935	J. A. Morales-Soto et al. (2021); A. Albert et al. (2022)
LHAASO	0.940	Z. Cao et al. (2024)
TUNKA-133	0.940	V. Prosin et al. (2014); V. V. Prosin et al. (2016)
Auger	1.00	P. Abreu et al. (2013, 2021)
IceCube-IceTop	0.935	M. G. Aartsen et al. (2019)
IceTop	0.970	M. G. Aartsen et al. (2020)
KASCADE	0.965	M. R. Finger (2011)
KASCADE-Grande	1.00	W. D. Apel et al. (2013)
TA	0.910	R. U. Abbasi et al. (2018a); D. Ivanov (2020)
TALE	0.99	R. U. Abbasi et al. (2018b, 2021)
Tibet-III	1.00	M. Amenomori et al. (2008)

To calibrate the energy scale of ground-based experiments affected by large systematic uncertainties, we use the positions of spectral features, such as the knee and the second knee, to obtain δ. First, we calibrate HAWC's energy scale using the proton–helium (p+He) spectrum as determined by DAMPE (F. Alemanno et al. 2024) and HAWC (A. Albert et al. 2022). Then, we calibrate the all-particle spectrum of LHAASO (Z. Cao et al. 2024) against that of HAWC (J. A. Morales-Soto et al. 2021). Following this, TUNKA-133's all-particle spectrum (V. Prosin et al. 2014) is calibrated using LHAASO. Finally, the all-particle spectrum of Auger (P. Abreu et al. 2021) is calibrated using TUNKA-133. Energy scales for the remaining experiments are then adjusted through comparisons of the all-particle spectrum. The calibration parameters for each ground-based experiment are summarized in Table 2.

2.2. Spectrum Modeling

2.2.1. Galactic Components

A. Contribution from a local source. Precise measurements have revealed hardening in the energy spectra of protons and helium nuclei around hundreds of GV, with a subsequent softening near $\sim$10 TV (Q. An et al. 2019; M. Aguilar et al. 2020; F. Alemanno et al. 2021), along with clear anisotropy patterns at these energies (see M. Ahlers & P. Mertsch 2017 and references therein). Notably, the phase of dipole anisotropies experiences a reversal at $\sim$100 TeV, coinciding with the amplitude reaching its minimum. Below 100 TeV, the phase aligns roughly with the local interstellar magnetic field, as indicated by IBEX data (N. A. Schwadron et al. 2014), while at higher energies, it shifts toward the Galactic center (GC) direction.

The effects of a local source could naturally account for both phenomena, as suggested in W. Liu et al. (2019), K. Fang et al. (2020), A.-f. Li et al. (2021), P.-p. Zhang et al. (2021), B.-Q. Qiao et al. (2022), and Y. Zhang et al. (2022). The key point is that the phase reversal stems from the competition between Galactic cosmic-ray (GCR) streamings: the background sources moving from the GC toward the anti-GC direction, dominating above 100 TeV, and the local source, from the source to its opposite, dominating below 100 TeV.

As previously outlined, the flux from the local source is phenomenologically described by a power-law spectrum with rigidity-dependent exponential cutoffs. Additionally, the propagation effect is taken into account that suppresses the local source's contribution at lower energies. Consequently, the contribution from the local source, denoted as $\Phi_{ls}(E)$, is modeled as follows:

$$\Phi_{ls}(E) = \sum_i \phi_{ls,i} \left(\frac{E}{\text{TeV}} \right)^{-\gamma_{ls,i}} \exp\left(-\frac{E}{Z E_{c,ls}} \right) \times \exp\left(-\frac{L^2}{4 D_{xx} \tau} \right), \quad (2)$$

where E represents the total energy, the sum extends over different primary particle types, $\phi_{ls,i}$ denotes the normalization, $\gamma_{ls,i}$ is the spectral index, Z is the atomic number, and $E_{c,ls}$ is the cutoff energy for protons. The local source's characteristics are defined by L (distance to the source), τ (age of the source), and $D_{xx} = D_0(R/4 \text{ GV})^\delta$ (the effective diffusion coefficient from the source to the solar system). We require a set of fiducial values to compute the local source's contribution. However, due to the unknown nature and high degeneracy of these parameters, determining them precisely is neither possible nor necessary. Consequently, we adopt the values from K. Fang et al. (2020), specifically $L = 500$ pc, $\tau = 2 \times 10^5$ yr, $D_0 = 5 \times 10^{27}$ cm^2 s^{-1}, and $\delta = 0.33$, while noting that this particular set of parameters has no special meaning.

B. Soft and hard background components. Different GCR components have already been considered in prior studies (V. I. Zatsepin & N. V. Sokolskaya 2006; R. Scrandis et al. 2021; T. K. Gaisser et al. 2013; C. Yue et al. 2019; Y. Zhang et al. 2022). This necessity arises because the spectral index before the hardening at hundreds of GV is notably soft (M. Aguilar et al. 2020). Assuming this to be the only background population, the all-particle spectrum would fall short of the measurements from ground-based experiments such as LHAASO (Z. Cao et al. 2024) from hundreds of TeV to the knee. Therefore, a second background population with a harder spectrum is required.

The diversity of GCR sources may account for the multiple GCR components. Possible GCR sources include different types of supernova remnants (SNRs; A. M. Hillas 2004, 2005), stellar clusters (W. Binns et al. 2008; F. Aharonian et al. 2019; T. Vieu & B. Reville 2022), and Wolf–Rayet star explosions (S. Thoudam et al. 2016). Additionally, CRs released at different SNR evolutionary phases could have different spectral indices and cutoff energies (Y. Zhang et al. 2017; Y. Zhang & S. Liu 2019). Furthermore, CRs that escaped into the Galactic

halo could be reaccelerated by the Galactic wind termination shocks (J. R. Jokipii & G. Morfill 1987; V. N. Zirakashvili & H. J. Völk 2006; S. Thoudam et al. 2016), potentially giving rise to a second population observed on Earth. It is noteworthy that propagation effects like spatially dependent diffusion (N. Tomassetti 2012; Y.-Q. Guo et al. 2016; M.-J. Zhao et al. 2021) can also cause a hardening of the background spectrum, mimicking the effect of two background populations.

Given the above considerations, we introduce two background populations alongside the contributions from the local source. The flux from each population is represented by

$$\Phi_a(E) = \sum_i \phi_{a,i} \left(\frac{E}{\text{TeV}}\right)^{-\gamma_{a,i}} \exp\left(-\frac{E}{ZE_{c,a}}\right), \qquad (3)$$

where Φ_a denotes the flux for population a (Pop. I/Pop. II) at total energy E, the sum extends over different primary particle types within population a, $\phi_{a,j}$ represents the normalization, $\gamma_{a,i}$ is the spectral index, Z is the atomic number, and $E_{c,a}$ is the cutoff energy for protons.

In the model, the predominant primaries include protons, helium, carbon, oxygen, nitrogen, magnesium, silicon, and iron. We also include a $Z = 53$ group in Pop. II, potentially originating from r-process nucleosynthesis (M. Arnould et al. 2007) as suggested in T. K. Gaisser et al. (2013). Other elements with lower abundances are neglected as they are not expected to have significant contributions to the total CR flux (J. J. Engelmann et al. 1990; M. Aguilar et al. 2020; N. E. Walsh 2020).

2.2.2. Extragalactic Components

In the modeling of extragalactic contributions, in addition to the use of power laws with rigidity-dependent exponential cutoffs, it is assumed that the extragalactic components are subject to exponential suppression at lower energies, consistent with the expectation of the "magnetic horizon effect" (T. Stanev et al. 2000; M. Lemoine 2005; V. Berezinsky & A. Z. Gazizov 2005b; S. Mollerach & E. Roulet 2013). Following the approach in S. Mollerach & E. Roulet (2019), the extragalactic component is modeled as

$$\Phi_{\text{xg}}(E) = \sum_i \phi_{\text{xg},i} \left(\frac{E}{100 \text{ PeV}}\right)^{-\gamma_{\text{xs},i}} \exp\left(-\frac{E}{ZE_{c,\text{xg}}}\right)$$
$$\times \frac{1}{\cosh(ZE_l/E)}, \qquad (4)$$

where E_l represents the characteristic energy scale below which the extragalactic contribution is suppressed. The $\cosh^{-1}(E_l/E)$ allows one to implement a smooth suppression of the spectrum without significantly affecting the spectral shape above $2ZE_l$. The parameterization of extragalactic fluxes is adopted as a pragmatic approach to ensure simplicity and clarity in the resulting model, as it does not account for propagation effects such as energy losses on CMB photons.

Identifying specific nuclei within the extragalactic components has always been challenging due to the limited statistics and complexities in mass composition reconstruction. In this study, we build upon the latest findings from the Pierre Auger Collaboration (F. Salamida 2023; A. Abdul Halim et al. 2023a, 2024), also reviewed in R. Aloisio (2023) and A. Coleman et al. (2023), summarized as follows. Above the

ankle, the proportion of protons is remarkably low.[8] Instead, the spectrum between the ankle and the cutoff is largely dominated by nuclei groups $2 \leqslant A \leqslant 4$ and $5 \leqslant A \leqslant 22$, as illustrated in Figure 9 in A. Abdul Halim et al. (2023a) and Figure 2 in A. Abdul Halim et al. (2024). Notably, the flux suppression observed at $E \sim 4 \times 10^{19}$ eV is ascribed to rigidity cutoffs at the cosmic source, rather than being a result of propagation effects (V. Berezinsky 2007).

Based on these findings, we assume the existence of two distinct extragalactic components. The HE component dominates the CR spectrum above the ankle and consists of helium and nitrogen, which correspond to the nuclear mass groups $2 \leqslant A \leqslant 4$ and $5 \leqslant A \leqslant 22$, respectively. Meanwhile, the LE component, contributing to the region between the knee and the ankle, consists of protons and helium, as suggested by R. Aloisio et al. (2014).

3. Results and Discussion

3.1. Spectra for Individual Species

The individual spectra of the major species, alongside the all-particle spectrum below the second knee, are shown in Figure 1, together with the data points used in the fitting process. The spectral parameters defining both the Galactic and extragalactic components are summarized in Table 3 and Table 4, respectively. Our model successfully reproduces most of the data sets within their respective error bars.

The three Galactic components in our model play distinct roles in shaping the primary CR spectrum. Pop. I, characterized by a soft spectrum with a cutoff at 30 TV, predominantly influences the spectrum up to the hardening observed at approximately 200 GV. The local source, with a cutoff at 36 TV, is primarily responsible for the bump observed in the proton and helium spectra around 10 TV. Pop. II, marked by a cutoff at 4.8 PV and a spectrum harder than that of Pop. I, contributes to the formation of the knee. Regarding the extragalactic components, the LE component, with a cutoff at 1 EV and a suppression below 19 PV, influences the spectrum between the LE ankle and the ankle. Conversely, the HE component, which cuts at 4 EV and attenuates below 1.5 EV, dominates the spectrum above the ankle.

A few data points appear to be systematically offset, indicating mild tension between different experiments that persists even after energy rescaling. Notably, the KASCADE experiment and its extension, KASCADE-Grande, provide comprehensive results for different CR element groups. Our model overpredicts the proton flux while underpredicting the iron flux in the energy range of 10^6–10^8 GeV. Consequently, our model aligns with the all-particle spectrum, as shown in the upper panel of Figure 2, while the predicted $\langle \ln A \rangle$ falls below their measurements, as illustrated in the lower panel of Figure 2. To reconcile our model with the KASCADE and KASCADE-Grande measurements, the Pop. II proton spectrum needs to be softer, while the Pop. II iron spectrum needs to be harder. Given that the present model is considerably influenced by the measurements of LHAASO $\langle \ln A \rangle$ data, we anticipate

---

[8] The reason why protons cannot dominate above the knee can be understood through the following rationale. The mean logarithmic mass rise from 10^{18} eV to 10^{20} eV eventually reaches $\langle \ln A \rangle \gtrsim 2.0$. If we hypothesize that protons constitute half of the spectrum, the other half would need to comprise heavier elements, like iron, to reproduce the $\langle \ln A \rangle$ measurements. However, such a composition would result in a significantly larger $\sigma(\ln A)$, which contradicts observations (P. Abreu et al. 2013).
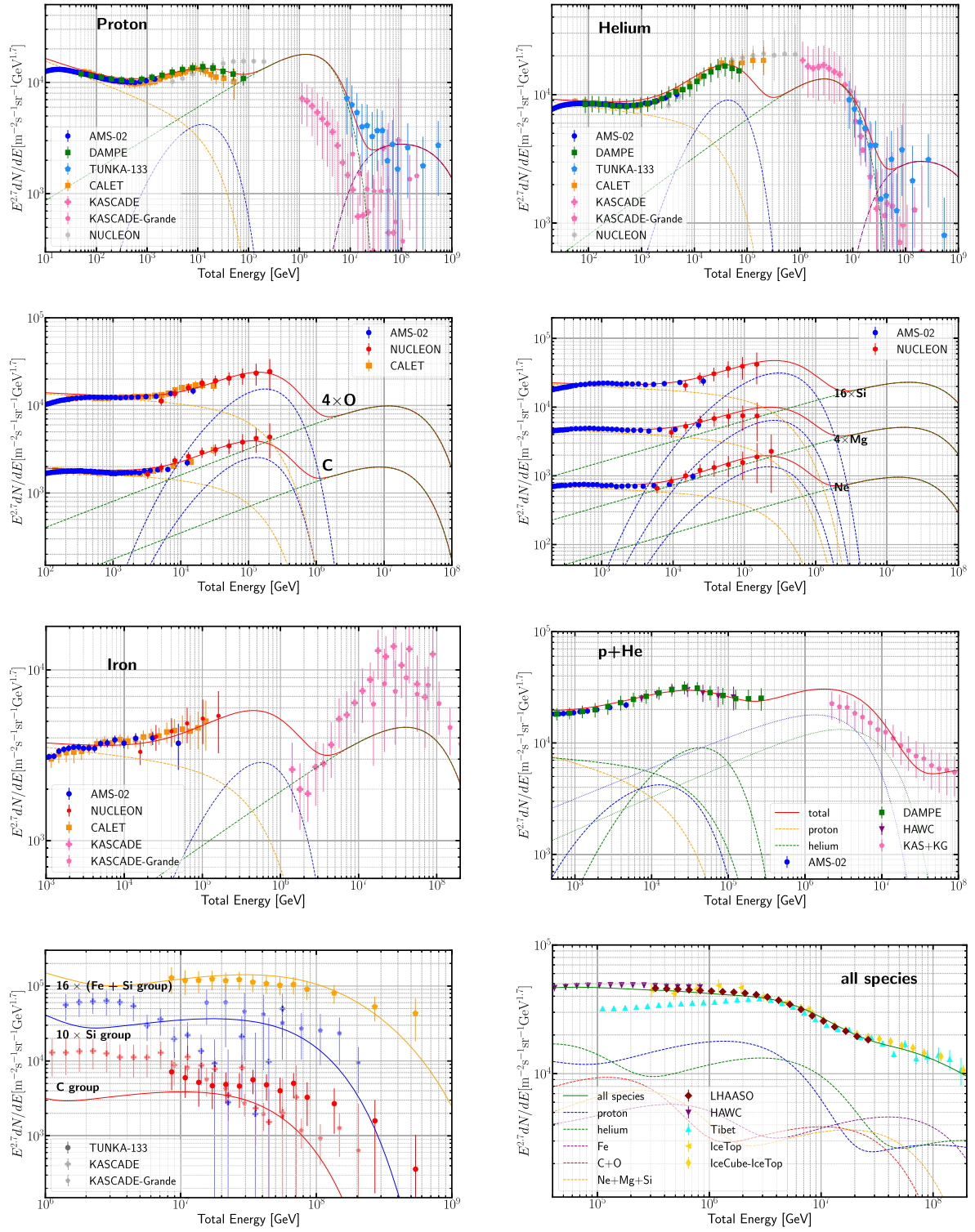
Figure 1. Fitted energy spectra of our model, compared with the data. In each panel, the orange, blue, and green dashed lines show the contributions of Pop. I, local source, and Pop. II, respectively, while the solid lines are the total contribution. References of the data: protons, AMS-02 (M. Aguilar et al. 2020), DAMPE (Q. An et al. 2019), TUNKA-133 (V. Prosin et al. 2014), CALET (O. Adriani et al. 2022), KASCADE and KASCADE-Grande (W. D. Apel et al. 2013); helium, AMS-02 (M. Aguilar et al. 2020), DAMPE (F. Alemanno et al. 2021), TUNKA-133 (V. Prosin et al. 2014), CALET (O. Adriani et al. 2023), KASCADE and KASCADE-Grande (W. D. Apel et al. 2013); carbon and oxygen, AMS-02 (M. Aguilar et al. 2020), NUCLEON (V. Grebenyuk et al. 2019), CALET (O. Adriani et al. 2020); neon, magnesium, and silicon, AMS-02 (M. Aguilar et al. 2020), NUCLEON (V. Grebenyuk et al. 2019); iron, AMS-02 (M. Aguilar et al. 2020), CALET (O. Adriani et al. 2021), KASCADE and KASCADE-Grande (W. D. Apel et al. 2013); p+He, AMS-02 (M. Aguilar et al. 2020), DAMPE (F. Alemanno et al. 2024), HAWC (A. Albert et al. 2022), KAS+KG (S. Schoo et al. 2016); groups, TUNKA-133 (V. Prosin et al. 2014), KASCADE and KASCADE-Grande (W. D. Apel et al. 2013); all-particle, LHAASO (Z. Cao et al. 2024), HAWC (J. A. Morales-Soto et al. 2021), Tibet (M. Amenomori et al. 2008), IceTop (M. G. Aartsen et al. 2020).

Table 3
Spectral Parameters of the Galactic Components

Species	Pop. I: $E_c = 30$ TV		Loc. Source: $E_c = 36$ TV		Pop. II: $E_c = 4.8$ PV	
	$\Phi_{0,i}$ (m^{-2} s^{-1} sr^{-1} GeV^{-1})	γ_i	$\Phi_{0,i}$ (m^{-2} s^{-1} sr^{-1} GeV^{-1})	γ_i	$\Phi_{0,i}$ (m^{-2} s^{-1} sr^{-1} GeV^{-1})	γ_i
p	5.4×10^{-5}	2.88	2.0×10^{-4}	2.77	2.5×10^{-5}	2.42
He	5.7×10^{-5}	2.75	1.5×10^{-4}	2.45	1.3×10^{-5}	2.40
C	1.3×10^{-5}	2.75	3.2×10^{-5}	2.45	1.0×10^{-6}	2.40
O	2.4×10^{-5}	2.75	4.5×10^{-5}	2.45	1.6×10^{-6}	2.40
Ne	5.2×10^{-6}	2.75	1.5×10^{-5}	2.45	5.8×10^{-7}	2.40
Mg	8.6×10^{-6}	2.75	1.7×10^{-5}	2.45	7.3×10^{-7}	2.40
Si	9.9×10^{-6}	2.75	2.0×10^{-5}	2.45	7.9×10^{-7}	2.40
Fe	2.8×10^{-5}	2.75	2.5×10^{-5}	2.45	1.7×10^{-6}	2.38
$Z = 53$	...	...	...	...	1.5×10^{-8}	2.10

Table 4
Spectral Parameters of the Extragalactic Components

Species	LE: $E_c = 1$ EV, $E_l = 19$ PV		HE: $E_c = 4$ EV, $E_l = 1.5$ EV	
	$\Phi_{0,i}$ (m^{-2} s^{-1} sr^{-1} GeV^{-1})	γ_i	$\Phi_{0,i}$ (m^{-2} s^{-1} sr^{-1} GeV^{-1})	γ_i
p	8.0×10^{-19}	2.67	...	
He	8.5×10^{-19}	2.67	3.1×10^{-20}	2.0
N	...	...	1.7×10^{-20}	2.0

that the future LHAASO measurements (L. Yin et al. 2023; Y. Zhiyong et al. 2023) will show higher proton fluxes and lower iron fluxes compared to the KASCADE results.

Another systematic offset is observed in the all-particle data measured by Tibet-III before the knee. In this energy range, the Tibet-III spectrum is harder than our model and other measurements, even accounting for the tens of percent systematic errors quoted in M. Amenomori et al. (2008). A generally harder Pop. II spectral index is needed to reproduce their results.

Lastly, it is worth mentioning that the data from CALET and NUCLEON do not demonstrate a dip around 300 TeV in the helium spectrum, in contrast to the observation made by DAMPE. To account for the CALET and NUCLEON helium data, a new component unique to helium is required, introducing more complexities to our existing model. However, this modification would not impact the other major findings outlined in our research.

3.2. All-particle Spectrum

The all-particle spectrum predicted by our model is illustrated in the upper panel of Figure 2. Our model accurately captures the major spectral features in the all-particle spectrum and the evolution of mass composition with energy. As before, our model successfully reproduces most of the data sets within the error bars, although a few deviations will be addressed subsequently.

The transition to extragalactic CRs in our model happens just above 10^{17} eV, in agreement with the findings in E. G. Berezhko & H. J. Voelk (2007), R. Aloisio et al. (2014), G. Giacinti et al. (2015), L. Sveshnikova et al. (2015), and S. Mollerach & E. Roulet (2019). However, there are suggestions that the extragalactic LE component, consisting of light elements, may have a Galactic origin, such as Wolf–Rayet stars, as proposed in S. Thoudam et al. (2016). In this scenario, the transition is close to the ankle, consistent with earlier beliefs (J. P. Rachen et al. 1993; T. Wibig & A. W. Wolfendale 2005; V. Berezinsky 2007).
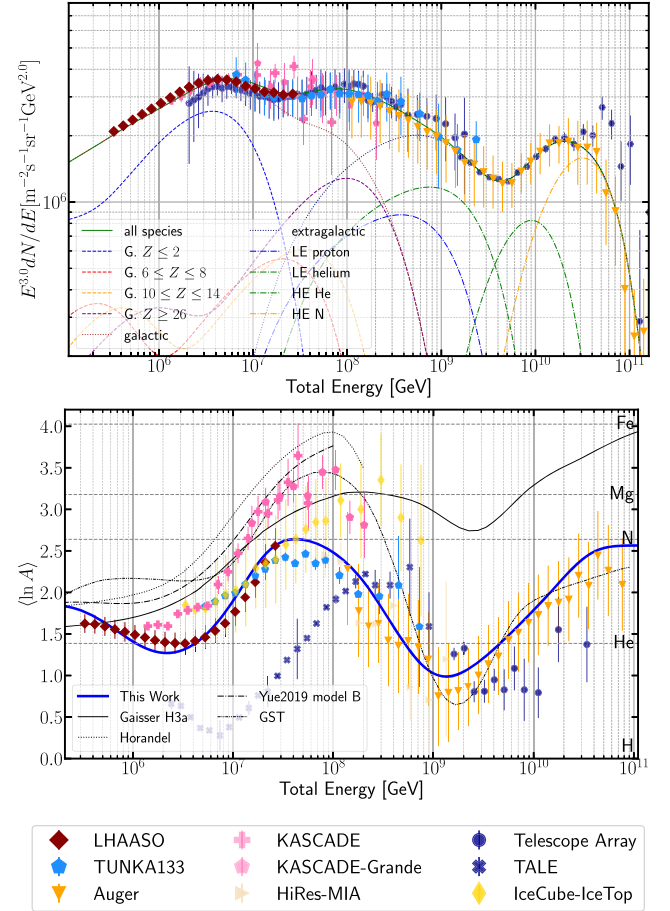

Figure 2. All-particle spectrum (upper panel) and the mean logarithmic mass (lower panel) from 2×10^{14} eV to 2×10^{11} eV. "G" stands for "galactic" in the upper panel. References: all-particle, LHAASO (Z. Cao et al. 2024), TUNKA-133 (V. Prosin et al. 2014), Auger (P. Abreu et al. 2021), TALE (R. U. Abbasi et al. 2018b), TA (D. Ivanov 2020), KASCADE (W. D. Apel et al. 2013), KASCADE-Grande (W. D. Apel et al. 2013); $\langle \ln A \rangle$, LHAASO (Z. Cao et al. 2024), TUNKA-133 (V. V. Prosin et al. 2016), Auger (P. Abreu et al. 2013), HiRes-MIA (K.-H. Kampert & M. Unger 2012), TALE (R. U. Abbasi et al. 2021), TA (R. U. Abbasi et al. 2018a), IceCube-IceTop (M. G. Aartsen et al. 2019), KASCADE (M. R. Finger 2011), KASCADE-Grande (W. D. Apel et al. 2013), Gaisser H3a (T. K. Gaisser et al. 2013), Horandel (J. R. Hörandel 2003), Yue2019 model B (C. Yue et al. 2019), GST (T. K. Gaisser et al. 2013). The other references are the same as in Figure 1.

The true nature of this additional component remains subject to debate. In our model, the LE cutoff occurs at a value lower than that proposed in certain prior studies (M. Lemoine 2005;

S. Mollerach & E. Roulet 2019), which suggests a cutoff around 100 PeV. However, the considerable uncertainties surrounding the intensity and configuration of the extragalactic magnetic field imply that this value is only loosely constrained. Another unresolved question is whether nearby sources can provide sufficient luminosity at tens of PeV, particularly given that the closest neighboring galaxies, such as M31, are known to exhibit relatively low levels of CR emissions. Nevertheless, the historical activities of these nearby galaxies could potentially yield a notable contribution at these energy levels (V. N. Zirakashvili et al. 2022). Conversely, attributing this component to Galactic origins presents challenges. The minimal level of observed anisotropy within the energy range of 10^{17}–10^{18} eV (A. Aab et al. 2020) disfavors a Galactic origin scenario (P. Abreu et al. 2012; G. Giacinti et al. 2012), as such a scenario would typically manifest in a higher amplitude of anisotropy than what has been observed. Furthermore, identifying a component with a cutoff at $\sim 10^{18}$ eV as Galactic poses significant obstacles related to the acceleration capabilities of Galactic sources (A. R. Bell 2013). Consequently, we designate this component as having an extragalactic origin within our current model while also acknowledging the possibility of alternative origins.

Next, we turn to the formation of various spectral features in our model. The spectral knee is attributed to the cutoff in the proton spectrum of Pop. II at 4.8 PeV. This feature is further broadened due to the cutoff in the helium spectrum, occurring at 9.6 PeV. Our findings align with those presented in H. P. Dembinski et al. (2018), Y.-Q. Guo & Q. Yuan (2018), and S. Mollerach & E. Roulet (2019), offering a contrast to earlier studies that suggested that the knee is dominated by nuclei heavier than helium (M. Shibata et al. 2010; Y. Zhao et al. 2015; S. Thoudam et al. 2016). The reason for a light knee originates from its mass composition, as measured by LHAASO (Z. Cao et al. 2024), where the mean logarithmic mass is heavier than He and lighter than CNO, suggesting that the first cutoff of the all-particle energy spectrum is attributed to lighter elements, rather than to medium–heavy elements.

The spectral hardening around 20 PeV, known as the LE ankle, is attributed to the increasing contribution of proton and helium from the LE component, as supported by recent studies (L. Sveshnikova et al. 2015; S. Mollerach & E. Roulet 2019). Specifically, the total Galactic contribution exhibits no significant hardening, as is apparent from the upper panel of Figure 2. This interpretation contrasts with earlier theories, such as those proposed in L. G. Sveshnikova et al. (2013), in which the hardening was due to the rise of heavy Galactic components contributing to the knee. The rationale for favoring an extra component is twofold. First, achieving such hardening would necessitate a substantially harder spectral index for medium–heavy elements compared to protons and helium, which is physically implausible at such high energies where the rest mass is negligible. Second, even if the spectral feature is reproduced, the resulting mean logarithmic mass around 20 PeV would be too high compared with LHAASO and TUNKA-133 measurements.

The second knee occurs at around 200 PeV in our model and is attributed to the steepening of the Galactic iron and elements in the $Z = 53$ group. This slightly contrasts with the findings from T. Abu-Zayyad et al. (2018) and S. Mollerach & E. Roulet (2019), who attribute the second knee exclusively to the steepening of Galactic iron. The discrepancy between these interpretations and ours stems from the preferred data sets: T. Abu-Zayyad et al. (2018) and S. Mollerach & E. Roulet (2019) rely on TALE data that locate the second knee at 100 PeV, whereas our analysis prioritizes Auger and TUNKA-133 data, which place the second knee at 200 PeV. Consequently, the ratio $E_{2^{nd} \text{knee}}/E_{\text{knee}}$ changes from ~ 26 (the atomic number of iron) in the former scenario to ~ 53 in the latter. Given the systematic errors at such high energies, no statistically significant tensions exist between these two data set choices. Reaching a definitive conclusion relies on future, more precise measurements.

Regarding the spectral region at and beyond the ankle, our model aligns with the findings of the Auger Collaboration (F. Salamida 2023; A. Abdul Halim et al. 2023a, 2024). Specifically, the helium and CNO nuclei, characterized by a notably hard spectrum[9] and a rigidity-dependent cutoff, are responsible for the formation of the ankle at ~ 5 EeV and the subsequent cutoff at ~ 40 EeV. The all-particle spectrum measured by TA is higher than that observed by Auger at the highest energies, a discrepancy confirmed by the joint Auger–TA working group (O. Deligny 2020; D. R. Bergman et al. 2024). However, this discrepancy arises at such high energies that it does not impact the main conclusions of this study. We refer the reader to P. Plotko et al. (2023) and references therein for a discussion of the possible reasons behind this mismatch.

3.3. The Mean Logarithmic Mass

As Hillas has demonstrated, "The smoothness of the total spectrum can hide large bumps in individual components" (A. M. Hillas 2006). Consequently, the crucial insights provided by the mean logarithmic mass are essential for the construction of our model. Our model's prediction of the mean logarithmic mass is shown in the lower panel of Figure 2, along with the prediction of previous models (J. R. Hörandel 2003; T. K. Gaisser et al. 2013; T. Stanev et al. 2014; C. Yue et al. 2019).

It can be seen in Figure 2 that the decreases in the mean logarithmic mass—the first decrease spanning 0.3–3 PeV, followed by a second decrease ranging from ~ 40 PeV to ~ 1 EeV—stem from similar origins. The cutoff in the local iron source naturally accounts for the first decrease in the mean logarithmic mass. This trend is evident in the lower left panel of Figure 1. The previous models (J. R. Hörandel 2003; T. K. Gaisser et al. 2013; T. Stanev et al. 2014; C. Yue et al. 2019) fail to depict this decrease, which demonstrates the importance of the Galactic local contribution included in our model. The second decrease in the mean logarithmic mass is associated with the cutoff of iron and $Z = 53$ group elements in the Pop. II component. In summary, both decreases in the average logarithmic mass result from the cutoff of the heavy elements, the former from the local source and the latter from the Pop. II component.

Likewise, the causes for the two observed rises in the mean logarithmic mass, with the first spanning from 0.3 to 40 PeV and the second starting at 1 EeV, are consistent. Both rises are primarily attributed to the cutoff of the proton contributions, the

---

[9] In our model, the spectral index for the HE component is set at -2.0, in contrast to the Auger Collaboration's findings, which suggest even harder indices, exceeding 1.0 (A. Abdul Halim et al. 2023a). This divergence arises because our model includes an LE suppression for the HE component at 4 EV, resulting in a notably steep overall spectrum.

former from the Galactic component and the latter from the LE component.

We notice the correlation between features in the energy spectrum and the mean logarithmic mass. The local source, which accounts for the 10 TV bump in the proton and helium spectrum, naturally leads to the observed decrease from 0.3 to 3 PeV, as measured by LHAASO. Similarly, the cutoff in the Galactic components, resulting in the knee, naturally accounts for the decrease observed by Auger. Therefore, the features in the spectrum and in the mean logarithmic mass are natural consequences of its multicomponent nature.

Despite the absence of significant tension among the measurements of $\langle \ln A \rangle$ across most experiments after accounting for systematic errors, the central values exhibit variations. Our model aligns well with the central values as measured by LHAASO, TUNKA-133, and Auger. Regarding other data sets, the TA results are consistent with those from Auger within statistical and systematic errors, as shown by the joint Auger–TA working group (A. Abdul Halim et al. 2023b). However, a fit to the TA data indicates a predominance of protons at the highest energies (D. Bergman 2021). Consequently, this suggests that our model's HE nitrogen component should be replaced by a proton component. The TALE measurement does not appear to agree with our model or any other measurements. While the results from KASCADE and IceCube-IceTop are consistent with our model considering their systematic errors, they may necessitate a softer Pop. II proton component and a harder Pop. II iron component, as discussed in Section 3.1.

4. Summary

The LHAASO Collaboration's measurements on the all-particle spectrum and the mean logarithmic mass with unprecedented precision are extremely important for understanding the origins of both Galactic and extragalactic CRs. In this study, we compile the latest data from multiple spaceborne and ground-based experiments and develop a phenomenological model based on this compilation. The incorporation of the multiple CR components in our model is based on measurements and guided by the principle of minimizing the introduction of new elements. Our model accurately reproduces all individual spectral measurements obtained from spaceborne experiments, alongside the all-particle spectrum and the mean logarithmic mass reported by ground-based experiments, covering the entire energy range between tens of GeV/Z and 10^{11} GeV. The different spectral features and various changes in $\langle \ln A \rangle$ are explained by the alternate contributions from different components. The main results obtained through this study indicate the following.

1. We find satisfactory agreement with the data by assuming three Galactic and two extragalactic components. In this work, we attribute the Galactic components to two background populations—one with a softer spectral index and the other with a harder spectral index—and a local source.
2. The spectral bump observed in the protons and the helium spectrum around 10 TV originates from an assumed local source's influence.
3. The presence of the knee at approximately 4 PeV is attributed to the cutoff of Galactic proton and helium contributions, indicating a light knee.
4. The emergence of the LE ankle near 20 PeV stems from the increasing contributions from the extragalactic protons and helium.
5. The formation of the second knee around 200 PeV is linked to the cutoff of the Galactic iron and potentially the elements within the $Z = 53$ group. The transition to extragalactic CRs happens just before the second knee.
6. The ankle hardening at $\sim$5 EeV is a purely extragalactic phenomenon, specifically, the contribution of an extremely hard HE extragalactic component composed of helium and CNO. The rigidity-dependent cutoff of this component results in the cutoff at $\sim$40 EeV.
7. Variations in the mean logarithmic mass share common causes: the decreases result from the cutoff of the heavy elements, initially by the local source followed by the Galactic component, whereas the rises are related to the cutoff of the proton contributions, initially from the Galactic and then from the LE component.

Upcoming measurements by LHAASO focusing on various CR groups (p, He, C, Si, Fe; L. Wang et al. 2023; L. Yin et al. 2023; S. Zhang 2023; Y. Zhiyong et al. 2023), with larger statistics and reduced systematic errors, will serve as a critical evaluation of our model. Our model predicts an iron knee near 500 TeV, similar to the structures observed in T. K. Gaisser et al. (2013) and H. P. Dembinski et al. (2018). Moreover, in our model, the fraction of iron in Pop. II is smaller than that in Pop. I: the Fe/He ratio is approximately 0.5 in Pop. I, while in Pop. II, it is $\sim$0.1. If Pop. I and Pop. II correspond to distinct source populations, this difference may provide intriguing insights into their nature.

The components required by our model could be associated with the various proposed CR sources. The LE CR background Pop. I quite possibly originate from SNRs, while the HE CR background Pop. II may originate from different sources, such as microquasars (S. Heinz & R. A. Sunyaev 2002; W. Bednarek 2005; G. J. Escobar et al. 2022), young massive stellar clusters (W. Binns et al. 2008; F. Aharonian et al. 2019; T. Vieu & B. Reville 2022), or even pulsar wind nebulae (K. S. Cheng et al. 1990; Y. Ohira et al. 2018; R.-Y. Liu & X.-Y. Wang 2021). The local source may be due to the Geminga SNR (P. A. Johnson 1994; B. Zhao et al. 2022, 2023). For the extragalactic components, the LE component may be contributed by nearby starburst galaxies (L. A. Anchordoqui et al. 1999; G. E. Romero et al. 2018), while the HE component may originate from active galactic nuclei (M. Ostrowski 2000; R. Mbarek & D. Caprioli 2019; X. Rodrigues et al. 2021).

Future work will build on these findings to refine our understanding of CR origins and propagation. Theoretically, adopting a more self-consistent approach (G. Schwefer et al. 2023) that begins with the sources and describes the observed spectra using diffusive transport, turbulence characterization, or the inclusion of multimessenger information could significantly clarify the physical implications of the parameters in our phenomenological model. Experimentally, developments in CR observational technology, such as the High Energy cosmic-Radiation Detector (P. W. Cattaneo 2019), the NeUtrino and Seismic Electromagnetic Signals space mission (M. Di Santo 2023), IceCube-Gen2 (M. G. Aartsen et al. 2021), and others, alongside advances in theoretical modeling, are set to deepen our understanding of CRs.

ORCID iDs

Xing-Jian Lv ⓘ https://orcid.org/0000-0002-5197-3393
Xiao-Jun Bi ⓘ https://orcid.org/0000-0002-5334-9754
Kun Fang ⓘ https://orcid.org/0000-0002-1209-349X
Yi-Qing Guo ⓘ https://orcid.org/0000-0003-4932-9619
Hui-Hai He ⓘ https://orcid.org/0000-0002-5963-4281
Qiang Yuan ⓘ https://orcid.org/0000-0003-4891-3186
Meng-Jie Zhao ⓘ https://orcid.org/0000-0001-6844-1409

References

Aab, A., Abreu, P., Aglietta, M., et al. 2020, ApJ, 891, 142
Aartsen, M. G., Abbasi, R., Abdou, Y., et al. 2013, PhRvD, 88, 042004
Aartsen, M. G., Abbasi, R., Ackermann, M., et al. 2020, PhRvD, 102, 122001
Aartsen, M. G., Abbasi, R., Ackermann, M., et al. 2021, JPhG, 48, 060501
Aartsen, M. G., Ackermann, M., Adams, J., et al. 2019, PhRvD, 100, 082002
Abbasi, R. U., Abe, M., Abu-Zayyad, T., et al. 2018a, ApJ, 858, 76
Abbasi, R. U., Abe, M., Abu-Zayyad, T., et al. 2018b, ApJ, 865, 74
Abbasi, R. U., Abe, M., Abu-Zayyad, T., et al. 2021, ApJ, 909, 178
Abdul Halim, A., Abreu, P., Aglietta, M., et al. 2023a, JCAP, 05, 024
Abdul Halim, A., Abreu, P., Aglietta, M., et al. 2023b, ICRC (Nagoya), 444, 249
Abdul Halim, A., Abreu, P., Aglietta, M., et al. 2024, JCAP, 01, 022
Abreu, P., Aglietta, M., Ahlers, M., et al. 2012, ApJL, 762, L13
Abreu, P., Aglietta, M., Ahlers, M., et al. 2013, JCAP, 02, 026
Abreu, P., Aglietta, M., Albury, J. M., et al. 2021, EPJC, 81, 966
Abu-Zayyad, T., Ivanov, D., Jui, C. C. H., et al. 2018, arXiv:1803.07052
Adriani, O., Akaike, Y., Asano, K., et al. 2020, PhRvL, 125, 251102
Adriani, O., Akaike, Y., Asano, K., et al. 2021, PhRvL, 126, 241101
Adriani, O., Akaike, Y., Asano, K., et al. 2022, PhRvL, 129, 101102
Adriani, O., Akaike, Y., Asano, K., et al. 2023, PhRvL, 130, 171002
Adriani, O., Barbarino, G. C., Bazilevskaya, G. A., et al. 2011, Sci, 332, 69
Adriani, O., Barbarino, G. C., Bazilevskaya, G. A., et al. 2016, ApJ, 818, 68
Aguilar, M., Aisa, D., Alpat, B., et al. 2015a, PhRvL, 115, 211101
Aguilar, M., Aisa, D., Alpat, B., et al. 2015b, PhRvL, 114, 171103
Aguilar, M., Ali Cavasonza, L., Ambrosi, G., et al. 2019, PhRvL, 123, 181102
Aguilar, M., Ali Cavasonza, L., Ambrosi, G., et al. 2021, PhR, 894, 1
Aharonian, F., Yang, R., & de Oña Wilhelmi, E. 2019, NatAs, 3, 561
Ahlers, M., & Mertsch, P. 2017, PrPNP, 94, 184
Ahn, H. S., Allison, P., Bagliesi, M. G., et al. 2010, ApJ, 714, L89
Albert, A., Alfaro, R., Alvarez, C., et al. 2022, PhRvD, 105, 063021
Alemanno, F., Altomare, C., An, Q., et al. 2024, PhRvD, 109, L121101
Alemanno, F., An, Q., Azzarello, P., et al. 2021, PhRvL, 126, 201102
Aloisio, R. 2023, JPhCS, 2429, 012008
Aloisio, R., Berezinsky, V., & Blasi, P. 2014, JCAP, 10, 020
Amenomori, M., Bi, X. J., Chen, D., et al. 2008, ApJ, 678, 1165
An, Q., Asfandiyarov, R., Azzarello, P., et al. 2019, SciA, 5, eaax3793
Anchordoqui, L. A., Romero, G. E., & Combi, J. A. 1999, PhRvD, 60, 103001
Apel, W. D., Arteaga-Velázquez, J. C., Bekk, K., et al. 2013, APh, 47, 54
Arnould, M., Goriely, S., & Takahashi, K. 2007, PhR, 450, 97
Atkin, E., Bulatov, V., Dorokhov, V., et al. 2018, JETPL, 108, 5
Batista, R. A., Biteau, J., Bustamante, M., et al. 2019, FrASS, 6, 23
Becker Tjus, J., & Merten, L. 2020, PhR, 872, 1
Bednarek, W. 2005, ApJ, 631, 466
Bell, A. R. 2013, APh, 43, 56
Berezhko, E. G., & Voelk, H. J. 2007, ApJL, 661, L175
Berezinsky, V. 2007, Ap&SS, 309, 453
Berezinsky, V., & Gazizov, A. Z. 2006, ApJ, 643, 8
Bergman, D. 2021, ICRC (Berlin), 395, 338
Bergman, D. R., & Belz, J. W. 2007, JPhG, 34, R359
Bergman, D. R., Deligny, O., Fenu, F., et al. 2024, ICRC (Nagoya), 444, 406
Binns, W., Wiedenbeck, M., Arnould, M., et al. 2008, NewAR, 52, 427
Cao, Z., Aharonian, F., Axikegu, et al. 2024, PhRvL, 132, 131002
Cattaneo, P. W. 2019, NPPP, 306, 85

Cheng, K. S., Cheung, T., Lau, M. M., Yu, K. N., & Kwok, P. W. 1990, JPhG, 16, 1115
Coleman, A., Eser, J., Mayotte, E., et al. 2023, APh, 149, 102819
Deligny, O. 2020, ICRC (Madison, WI), 358, 234
Dembinski, H., Ongmongkolkul, P., Deil, C., et al. 2024, scikit-hep/iminuit, Version v2.25.2, Zenodo, doi:10.5281/zenodo.10638795
Dembinski, H. P., Engel, R., Fedynitch, A., et al. 2018, ICRC (Busan), 301, 533
Di Santo, M. 2023, IJMPS, 51, 2361004
Drury, L. O. 1983, RPPh, 46, 973
Engelmann, J. J., Ferrando, P., Soutoul, A., Goret, P., & Juliusson, E. 1990, A&A, 233, 96
Escobar, G. J., Pellizza, L. J., & Romero, G. E. 2022, A&A, 665, A145
Fang, K., Bi, X.-J., & Yin, P.-F. 2020, ApJ, 903, 69
Finger, M. R. 2011, PhD thesis, Karlsruhe Institute of Technology
Gaisser, T. K., Stanev, T., & Tilav, S. 2013, FrPhy, 8, 748
Giacinti, G., Kachelrieß, M., & Semikoz, D. V. 2015, PhRvD, 91, 083009
Giacinti, G., Kachelrieß, M., Semikoz, D. V., & Sigl, G. 2012, JCAP, 07, 031
Grebenyuk, V., Karmanov, D., Kovalev, I., et al. 2019, AdSpR, 64, 2546
Guo, Y.-Q., Tian, Z., & Jin, C. 2016, ApJ, 819, 54
Guo, Y.-Q., & Yuan, Q. 2018, ChPhC, 42, 075103
Heinz, S., & Sunyaev, R. A. 2002, A&A, 390, 751
Hess, V. F. 1912, PhyZ, 13, 1084, https://inspirehep.net/files/880fc3b9087fcfc846fab1e79df5b8eb
Hillas, A. M. 2004, NuPhS, 136, 139
Hillas, A. M. 2005, JPhG, 31, R95
Hillas, A. M. 2006, arXiv:astro-ph/0607109
Hörandel, J. R. 2003, APh, 19, 193
Ivanov, D. 2020, ICRC (Madison, WI), 358, 298
James, F., & Roos, M. 1975, CoPhC, 10, 343
Johnson, P. A. 1994, APh, 2, 257
Jokipii, J. R., & Morfill, G. 1987, ApJ, 312, 170
Kampert, K.-H., & Unger, M. 2012, APh, 35, 660
Lemoine, M. 2005, PhRvD, 71, 083007
Li, A.-f., Yuan, Q., Liu, W., & Guo, Y.-q. 2021, ApJ, 962, 43
Liu, R.-Y., & Wang, X.-Y. 2021, ApJ, 922, 221
Liu, W., Guo, Y.-Q., & Yuan, Q. 2019, JCAP, 10, 010
Mayotte, E. W., Abreu, P., Aglietta, M., et al. 2023, ICRC (Nagoya), 444, 365
Mbarek, R., & Caprioli, D. 2019, ApJ, 886, 8
Mollerach, S., & Roulet, E. 2013, JCAP, 2013, 013013
Mollerach, S., & Roulet, E. 2019, JCAP, 03, 017
Morales-Soto, J. A., Arteaga-Velázquez, J. C., Abeysekara, A. U., et al. 2021, ICRC (Berlin), 395, 330
Ohira, Y., Kisaka, S., & Yamazaki, R. 2018, MNRAS, 478, 926
Ostrowski, M. 2000, MNRAS, 312, 579
Panov, A. D., Adams, J. H., Jr., Ahn, H. S., et al. 2007, BRASP, 71, 494
Panov, A. D., Adams, J. H., Jr., Ahn, H. S., et al. 2009, BRASP, 73, 564
Peters, B. 1961, NCim, 22, 800
Plotko, P., van Vliet, A., Rodrigues, X., & Winter, W. 2023, ApJ, 953, 129
Potgieter, M. S. 2013, LRSP, 10, 3
Prosin, V., Berezhnev, S. F., Chiavassa, A., et al. 2014, NIMPA, 756, 94
Prosin, V. V., Berezhnev, S. F., Budnev, N. M., et al. 2016, in EPJ Web Conf. 121, Roma Int. Conf. on Astroparticle Physics, ed. P. Piattelli et al. (Les Ulis: EDP Sciences), 03004
Qiao, B.-Q., Luo, Q., Yuan, Q., & Guo, Y.-Q. 2022, ApJ, 942, 13
Rachen, J. P., Stanev, T., & Biermann, P. L. 1993, A&A, 273, 377
Rodrigues, X., Heinze, J., Palladino, A., van Vliet, A., & Winter, W. 2021, PhRvL, 126, 191101
Romero, G. E., Müller, A. L., & Roth, M. 2018, A&A, 616, A57
Salamida, F. 2023, arXiv:2312.14673
Schoo, S., Apel, W. D., Arteaga-Velazquez, J. C., et al. 2016, ICRC (The Hague), 236, 263
Schwadron, N. A., Adams, F. C., Christian, E. R., et al. 2014, Sci, 343, 988
Schwefer, G., Mertsch, P., & Wiebusch, C. 2023, ApJ, 949, 16
Scrandis, R., Bowman, D. P., & Seo, E.-S. 2021, ICRC (Berlin), 395, 1220
Shibata, M., Katayose, Y., Huang, J., & Chen, D. 2010, ApJ, 716, 1076
Stanev, T., Engel, R., Mucke, A., Protheroe, R. J., & Rachen, J. P. 2000, PhRvD, 62, 093005
Stanev, T., Gaisser, T. K., & Tilav, S. 2014, NIMPA, 742, 42
Strong, A. W., Moskalenko, I. V., & Ptuskin, V. S. 2007, ARNPS, 57, 285
Sveshnikova, L., Kuzmichev, L., Korosteleva, E., Prosin, V., & Ptuskin, V. S. 2015, NuPhS, 256, 218
Sveshnikova, L. G., Korosteleva, E. E., Kuzmichev, L. A., et al. 2013, JPhCS, 409, 012062
Thoudam, S., Rachen, J. P., van Vliet, A., et al. 2016, A&A, 595, A33
Tomassetti, N. 2012, ApJL, 752, L13

Vieu, T., & Reville, B. 2022, MNRAS, 519, 136
Walsh, N. E. 2020, PhD thesis, Washington Univ., St. Louis
Wang, L., Ma, L. L., Zhang, S., & Feng, C. 2023, ICRC (Nagoya), 444, 413
Wibig, T., & Wolfendale, A. W. 2005, JPhG, 31, 255
Yin, L., Chen, S., & Zhang, S. 2023, ICRC (Nagoya), 444, 419
Yoon, Y. S., Anderson, T., Barrau, A., et al. 2017, ApJ, 839, 5
Yue, C., Ma, P.-X., Yuan, Q., et al. 2019, FrPhy, 15, 24601
Zatsepin, V. I., & Sokolskaya, N. V. 2006, A&A, 458, 1
Zhang, P.-p., Qiao, B.-q., Liu, W., et al. 2021, JCAP, 05, 012
Zhang, S. 2023, ICRC (Nagoya), 444, 408

Zhang, Y., & Liu, S. 2019, MNRAS, 482, 5268
Zhang, Y., Liu, S., & Yuan, Q. 2017, ApJL, 844, L3
Zhang, Y., Liu, S., & Zeng, H. 2022, MNRAS, 511, 6218
Zhao, B., Guo, Y., & Zhou, X. 2023, Univ, 9, 93
Zhao, B., Liu, W., Yuan, Q., et al. 2022, ApJ, 926, 41
Zhao, M.-J., Fang, K., & Bi, X.-J. 2021, PhRvD, 104, 123001
Zhao, Y., Jia, H.-Y., & Zhu, F.-R. 2015, ChPhC, 39, 125001
Zhiyong, Y., Shoushan, Z., Liqiao, Y., et al. 2023, ICRC (Nagoya), 444, 423
Zirakashvili, V. N., Ptuskin, V. S., & Rogovaya, S. I. 2022, MNRAS, 519, L5
Zirakashvili, V. N., & Völk, H. J. 2006, AdSpR, 37, 1923